nature electronics

SUPPLEMENTARY INFORMATION
https://doi.org/10.1038/s41928-019-0305-3

In the format provided by the authors and unedited.

An ultrathin integrated nanoelectromechanical transducer based on hafnium zirconium oxide

Mayur Ghatge, Glen Walters, Toshikazu Nishida and Roozbeh Tabrizian*

Electrical and Computer Engineering Department, University of Florida, Gainesville, FL, USA. *e-mail: rtabrizian@ufl.edu

SECTION 1

A) Device Fabrication:

Figure 1 summarizes the fabrication process flow for implementation of the 70nm Si nanomechanical resonators actuated using 10nm Hafnium Zirconium Oxide ($Hf_{0.5}Zr_{0.5}O_2$) film. An ALD 30nm titanium nitride (TiN) / 10nm $Hf_{0.5}Zr_{0.5}O_2$ / 10nm TiN stack is grown on top of a 70nm device layer SOI substrate. ALD $Hf_{0.5}Zr_{0.5}O_2$ is grown via a Cambridge Nano Fiji 200 ALD system by alternating tetrakis(dimethylamido)hafnium(IV) and tetrakis(dimethylamido)zirconium(IV) precursors. Between each tetrakis(dimethylamido)hafnium(IV) and tetrakis(dimethylamido)zirconium(IV) pulses, H_2O pulse serves as the oxidizing source. With the substrate growth temperature at ~200^{0}C, a growth rate of ~1Å per HfO_2 and ZrO_2 cycle allows precise control over the layering and thickness profile. 30nm bottom TiN serves as the bottom electrode for the ferroelectric transducer while the top 10nm TiN serves as the capping electrode. TiN deposition was performed *in situ* utilizing tetrakis(dimethylamido)titanium(IV) and nitrogen plasma. ~20nm platinum (Pt) is sputtered on top of the capping electrode to serve as $RF_{in/out}$ electrodes for the two-port resonator. The top TiN layer is selectively patterned using Cl_2/H_2 based plasma process followed by etching of $Hf_{0.5}Zr_{0.5}O_2$ in BOE. To stabilize the orthorhombic phase a rapid thermal anneal (RTA) was performed at 500°C for 20s in N_2 environment. The capping TiN electrode helps promote the ferroelectric orthorhombic phase and suppress the non-ferroelectric monoclinic phase during the RTA process. Post RTA, the device geometry is defined by etching the bottom TiN using RIE process. The device is finally released from the backside by etching the handle layer and buried oxide (BOX) using DRIE and RIE respectively. Figure 2 and Figure 3 demonstrate the cross-sectional schematic of the $Hf_{0.5}Zr_{0.5}O_2$ transduced Si and AlN-on-Si nanomechanical resonator, respectively.

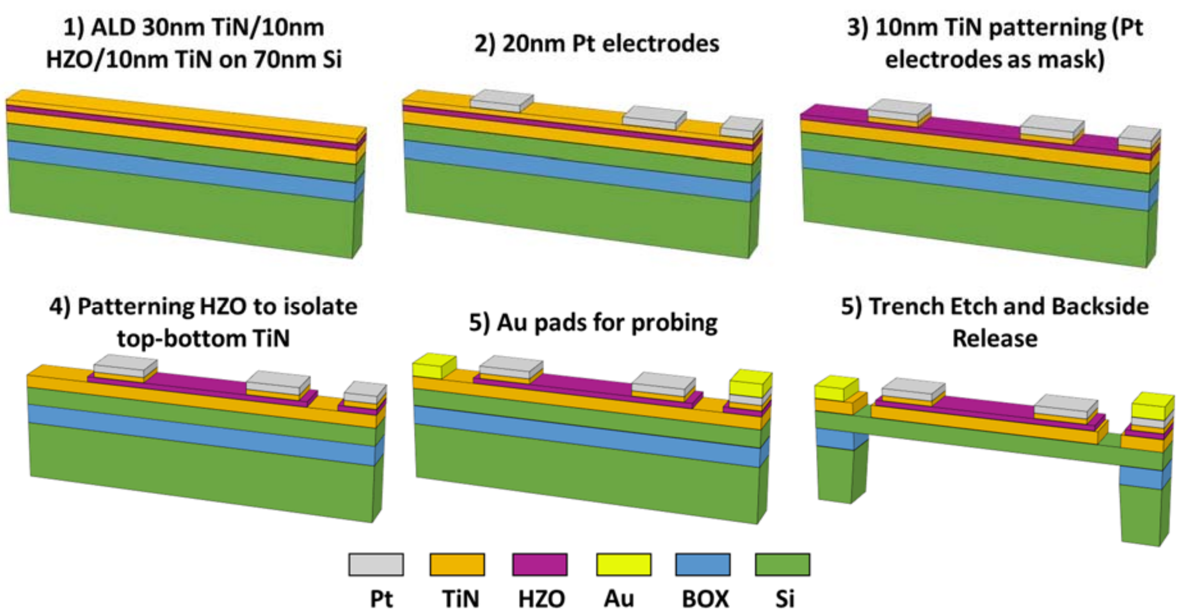

Figure 1 : Fabrication Process flow for $Hf_{0.5}Zr_{0.5}O_2$ (HZO)-on-Si devices

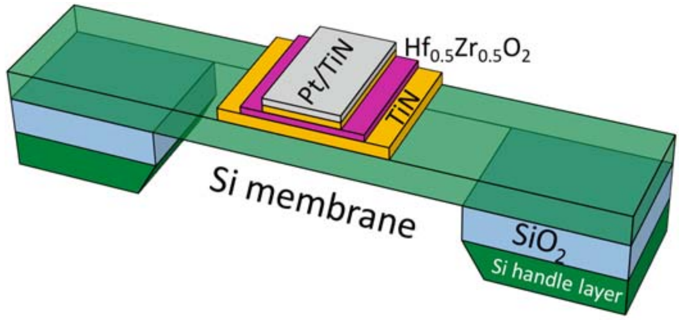

Figure 2: The cross-sectional schematic of the $Hf_{0.5}Zr_{0.5}O_2$ transduced Si nanomechanical resonator.

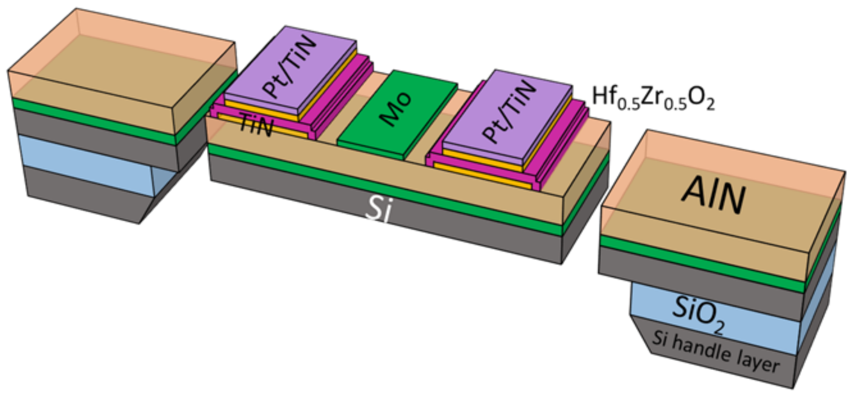

Figure 3: The cross-sectional schematic of the $Hf_{0.5}Zr_{0.5}O_2$ transduced AlN-on-Si nanomechanical resonator.

B) Electrical Characterization and Polarization Switching for $Hf_{0.5}Zr_{0.5}O_2$

Standard hysteresis measurement is achieved with a Sawyer-Tower circuit, while polarization switching is measured on a much faster time scale (more representative of device operation) by replacing the sense capacitor in the Sawyer-Tower circuit with a resistor and then pulsing the ferro-cap with µs square-wave pulses [40]. From this Positive-Up-Negative-Down (PUND) test, pulses can be applied, and the measured voltage integrated over time to obtain the positive switched (P), positive un-switched (U), negative switched (N), and negative un-switched (D) polarizations. Furthermore, polarization retention is extracted by subtracting the un-switched from the switched polarization (i.e. P-U and N-D). Conventionally, P-state denotes positive polarization and N-state denotes negative polarization state.

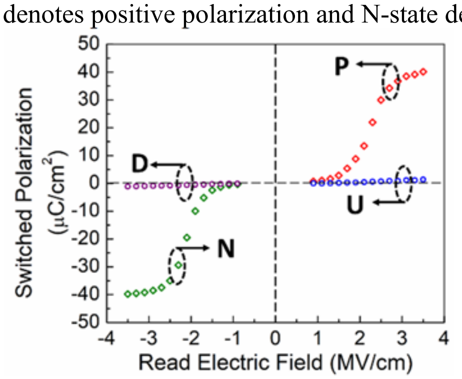

Figure 4 : Partial reads or variable voltage read pulses of 10nm $Hf_{0.5}Zr_{0.5}O_2$ devices.

Figure 4 shows the partial switching curve of the 10 nm $Hf_{0.5}Zr_{0.5}O_2$ films. Most of the polarization switching occurs between 2-3 MV/cm and saturates past 3 MV/cm and thus applying lower Electric fields (< 3MV/cm) leads to partial polarization/switching of domains. To read the polarization state of the film, read voltages at and below 3.5 MV/cm are applied, and this ensures minimal switching of the ferroelectric domains while confirming the polarization state. Figure 5 shows the PUND retention and ferroelectric domain switching for capacitors with d.c. bias/poling. In Figure 5 (a, b), a 1s d.c. write voltage ($+/-3.5V$) is applied. Poling the film with +3.5$V_{d.c.}$ polarizes the film in P-state while applying -3.5$V_{d.c.}$ switches the film polarization to N-state. The state of the ferroelectric polarization is read with a 12μs square-wave read pulse and the retention is demonstrated by the P-U and N-D values. These results showcase ferroelectric switching through d.c. biasing/poling.

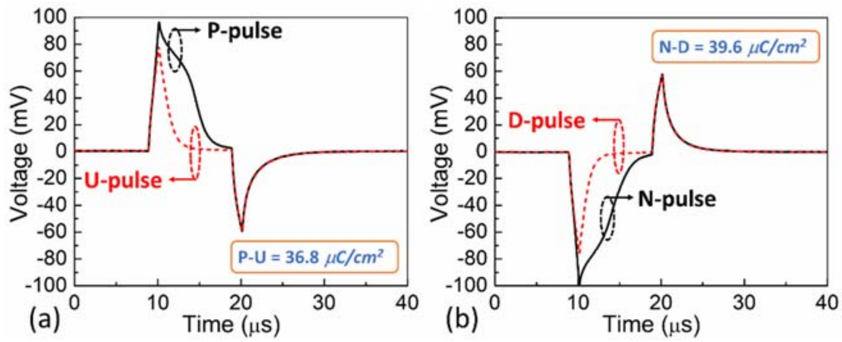

Figure 5: PUND read pulses after data writes performed with d.c. poling for 1s.

C) Device Characterization:

Optical characterization of the device is performed using the digital holographic microscope (DHM) to measure the RF performance of the device under different states of ferroelectric polarization. The device is actuated by applying $V_{d.c.}+V_{a.c.}$ to the RF_{in} port and the out-of-plane vibration amplitude is captured optically using the DHM. From the time-sequenced data captured using DHM, frequency response is extracted to measure the resonator performance. Apart from optical characterization, 2-port electrical characterization is performed to measure the transmission response with increasing input power. The electromechanical scattering phenomenon is observed by actuating the $Hf_{0.5}Zr_{0.5}O_2$ – transduced resonator using a signal generator at f_0 and measuring the double-sided power spectral density at f_0, $2f_0$ and $3f_0$.

SECTION 2

Electrostrictive Effect in Ferroelectric Materials:

Electrostriction plays an important role in the electromechanical behavior in ferroelectrics and describes the relation between polarization-induced strain (ε_i) and the spontaneous polarization ($P_j(\vec{E})$) as:

$$\varepsilon_i = Q_{ij}\left(P_j(\vec{E})\right)^2 \quad (1),$$

where, Q_{ij} are the electrostrictive coefficients. With the spontaneous polarization (P_j) related to the applied electric field ($\vec{E}$) through the non-linear polarization-electric field curve as shown in Figure 6, the polarization-induced strain (ε_i) results in the electromechanical phenomenon in ferroelectric materials.

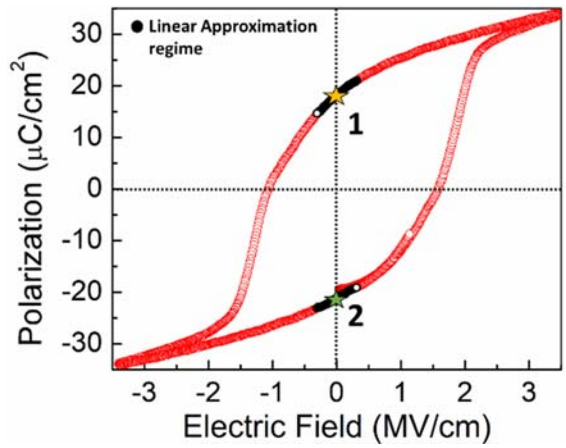

Figure 6: Polarization-electric field response of ferroelectric $Hf_{0.5}Zr_{0.5}O_2$. Linear approximation regime of the polarization-electric field relation is highlighted in black.

The linear electromechanical effect in ferroelectrics can be more generally expressed using the conventional d_{ij} piezoelectric coefficients which can be expressed as derivative of induced-strain with respect to the electric field:

$$d_{ij,linear} = \frac{\partial \varepsilon_i}{\partial E} = 2Q_{ij}P_j\frac{\partial P_j(\vec{E})}{\partial E} \qquad (2)$$

For $Hf_{0.5}Zr_{0.5}O_2$ ferroelectric transducers, the film is polarized through application of 3.5MV/cm electric field for ~1s to retain the film in state-1. Electromechanical phenomenon and the resulting piezoelectric coefficient for the $Hf_{0.5}Zr_{0.5}O_2$ transducer operating in state-1 is given by:

$$d_{ij,state-1} = 2Q_{ij}\epsilon_{ij}|P_0| \qquad (3)$$

where, ϵ_{ij} is the dielectric permittivity and $P_j = P_0 + \epsilon E_j$, is the linear approximation of the relation between the polarization density and the electric field. Owing to large dielectric permittivity and large remnant polarization (P_0) in state-1, a large piezoelectric coefficient is observed for $Hf_{0.5}Zr_{0.5}O_2$.

On the contrary, poling the film with -3.5MV/cm electric field for ~1s retains the film in state-2 resulting in a linear approximation of the piezoelectric coefficient having same magnitude but reversed polarity as state-1:

$$d_{ij,state-2} = -2Q_{ij}\epsilon_{ij}|P_0| \qquad (4)$$

The capability to inverse the polarization of the electromechanical transducer with d.c.-poling (see methods) invokes the possibility to operate the $Hf_{0.5}Zr_{0.5}O_2$ ferroelectric transducer not just in p-/n-state (state- 1 & 2 in Figure 6) but at multiple states of operation on the non-linear hysteresis loop as and when desired. This nonlinear hysteresis behavior leads to exciting avenues for nonlinear piezoelectricity. However, for $Hf_{0.5}Zr_{0.5}O_2$, there is no direct closed-form relation between P and E due to the nonlinear hysteresis behavior of the ferroelectric film.

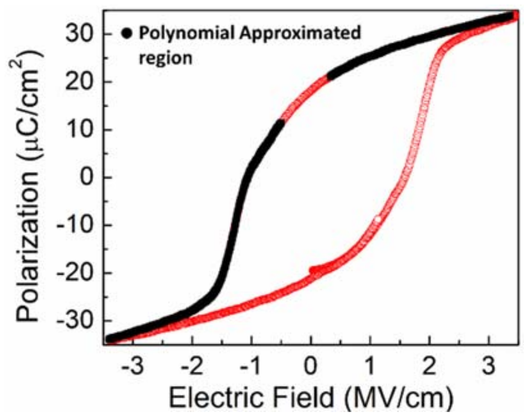

Figure 7: Polarization-electric field response of ferroelectric $Hf_{0.5}Zr_{0.5}O_2$. Piece-wise polynomial approximation region of the P-V relation is highlighted in black.

The spontaneous polarization-electric field relation shown in Figure 7 can be represented by a piece-wise polynomial approximation as:

$$P_j \cong P_0(1 + \epsilon_{ij}E_j + \epsilon'_{ij}{E_j}^2 + \epsilon''_{ij}{E_j}^3 + \ \ldots) \quad (5)$$

where, $\epsilon_{ij}, \epsilon'_{ij}, \cdots$ are the dielectric coefficients for the nonlinear relation between P_j and E_j. The electrostrictive effect can be further represented as:

$$\varepsilon_i = Q_{ij}\left(P_0(1 + \epsilon_{ij}E_j + \epsilon'_{ij}{E_j}^2 + \epsilon''_{ij}{E_j}^3 + \ \ldots)\right)^2 \quad (6)$$

thus, leading to mechanical strain at twice the excitation frequency. With $E_j = E_{\text{a.c.}} = V_o sin(\omega_0 t)$ being the input excitation a.c. signal, apart from the mechanical strain induced due to linear transduction at ω_0, nonlinear electrostrictive effect and nonlinear P-V relation leads to higher order harmonic generation at $2\omega_0$ and so on.
This nonlinear relation also results in a nonlinear electric field dependent piezoelectric coefficient given by:

$$d_{ij,non-linear} = 2Q_{ij}P_j(\epsilon_{ij} + \epsilon'_{ij}E_j + \epsilon''_{ij}{E_j}^2 + \ \ldots) \quad (7)$$

As evident in (7), the piezoelectric coefficient is directly proportional to the spontaneous polarization (P_j), and can be controlled with an applied electric field (E_j).

SECTION 3

Frequency-Quality factor (fQ) Figure of Merit in Nano-Mechanical Resonators:

Nano-mechanical resonators based on suspended membranes / cantilever beams of graphene, transition metal dichalcogenides, silicon carbide, silicon nitride and other novel 2D materials have been reported [41-61]. Below is the table summarizing the fQ product of various nano-mechanical resonators compared to the presented atomically engineered hafnium zirconium oxide ($Hf_{0.5}Zr_{0.5}O_2$) resonator that is operating at 12.8 GHz. Most of the reported nano-mechanical resonators are operating at low-frequency flexural modes and rely on non-integrated transduction schemes that limit vibration excitation and detection to low frequencies. As the mechanical vibrations scale to super- and extremely-high-frequency regimes (SHF: 3-30 GHz and EHF: 30-300GHz), the wavelength of harmonic strain perturbations, which defines the vibration pattern, scales down to few nanometers. Excitation and detection of harmonic perturbations with such small wavelengths is nearly impossible with available non-integrated schemes. On the contrary, the proposed $Hf_{0.5}Zr_{0.5}O_2$-based nano-mechanical resonators benefit from integrated transduction enabled by the electrostrictive effect in the ferroelectric $Hf_{0.5}Zr_{0.5}O_2$ film; hence, can be radically miniaturized in size to scale their operation frequency to SHF and EHF regimes. Figure 8 compares the fQ figure of merit for the 12.8 GHz $Hf_{0.5}Zr_{0.5}O_2$-based resonator with recently reported state-of-the-art nano-mechanical resonators [41-61].

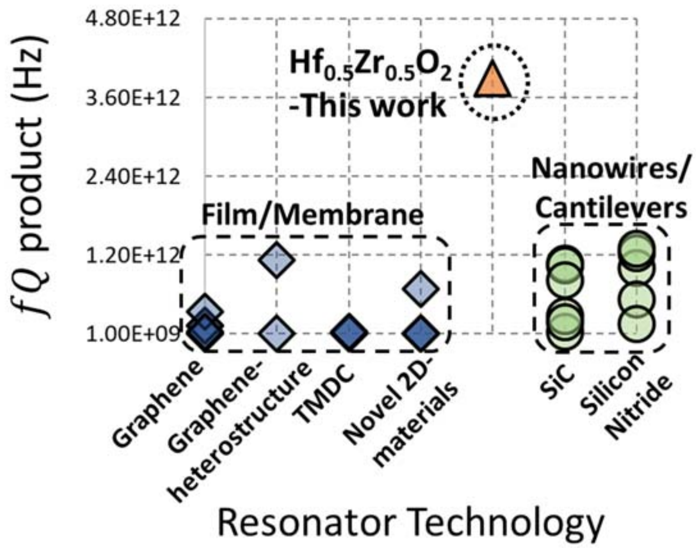

Figure 8: The fQ product figure of merit of the recently demonstrated state-of-the-art nano-mechanical resonators.

References:

[40] Rodriguez, J. A., et al. Reliability properties of low-voltage ferroelectric capacitors and memory arrays. *IEEE Transactions on Device and Materials Reliability,* ***4****(3), 436-449 (2004).*

[41] Lee, J., Wang, Z., He, K., Shan, J., & Feng, P.X.L. High frequency MoS2 nanomechanical resonators. *ACS nano,* ***7****(7), 6086-6091 (2013).*

[42] Islam, A., Lee, J., & Feng, P.X.L. All-electrical transduction of black phosphorus tunable 2D nanoelectromechanical resonators. *In 2018 IEEE Micro Electro Mechanical Systems (MEMS) (pp. 1052-1055). IEEE (2018, January).*

[43] Zheng, X.Q., et al. Beta gallium oxide (β-Ga2O3) nanoelectromechanical transducer for dual-modality solar-blind ultraviolet light detection. *APL Materials,* ***7****(2), 022523 (2019).*

[44] Ye, F., Lee, J., & Feng, P.X.L. Atomic layer MoS2-graphene van der Waals heterostructure nanomechanical resonators. *Nanoscale,* ***9****(46), 18208-18215 (2017).*

[45] Qian, Z., Hui, Y., Liu, F., Kai, S., & Rinaldi, M. 1.27 GHz Graphene-Aluminum Nitride nano plate resonant infrared detector. *In 2015 Transducers-2015 18th International Conference on Solid-State Sensors, Actuators and Microsystems (TRANSDUCERS) (pp. 1429-1432). IEEE (2015, June).*

[46] Castellanos-Gomez, A., et al. Single-Layer MoS2 Mechanical Resonators. *Advanced Materials,* ***25****(46), 6719-6723 (2013).*

[47] Bunch, J. S., et al. Electromechanical resonators from graphene sheets. *Science,* ***315****(5811), 490-493 (2007).*

[48] Wang, Z., et al. Black phosphorus nanoelectromechanical resonators vibrating at very high frequencies. *Nanoscale,* ***7****(3), 877-884 (2015).*

[49] Jia, H., et al. Single-and few-layer transfer-printed CVD MoS 2 nanomechanical resonators with enhancement by thermal annealing. *In 2016 IEEE International Frequency Control Symposium (IFCS) (pp. 1-3). IEEE (2016, May).*

[50] Jia, H., et al. Large-scale arrays of single-and few-layer MoS 2 nanomechanical resonators. *Nanoscale,* ***8****(20), 10677-10685 (2016).*

[51] Singh, R., Nicholl, R.J., Bolotin, K.I., & Ghosh, S. Motion transduction with thermo-mechanically squeezed graphene resonator modes. *Nano letters,* ***18****(11), 6719-6724 (2018).*

[52] Miller, D., & Alemán, B. Shape tailoring to enhance and tune the properties of graphene nanomechanical resonators. *2D Materials,* ***4****(2), 025101 (2017).*

[53] Zheng, X.Q., et al. β-Ga 2 O 3 NEMS Oscillator for Real-Time Middle Ultraviolet (MUV) Light Detection. *IEEE Electron Device Letters,* ***39****(8), 1230-1233 (2018).*

[54] Zheng, X.Q., Lee, J., Rafique, S., Zhao, H., & Feng, P.X.L Nanoelectromechanical Resonators Enabled by Si-Doped Semiconducting β-Ga 2 O 3 Nanobelts. *In 2018 IEEE International Frequency Control Symposium (IFCS) (pp. 1-2). IEEE (2018, May).*
[55] Oshidari, Y., Hatakeyama, T., Kometani, R., Warisawa, S.I., & Ishihara, S. High quality factor graphene resonator fabrication using resist shrinkage-induced strain. *Applied Physics Express, **5**(11), 117201 (2012).*
[56] Xu, Y., et al. Radio frequency electrical transduction of graphene mechanical resonators. *Applied Physics Letters, **97**(24), 243111 (2010).*
[57] Feng, P.X.L., White, C.J., Hajimiri, A., & Roukes, M.L. A self-sustaining ultrahigh-frequency nanoelectromechanical oscillator. *Nature nanotechnology, **3**(6), 342 (2008).*
[58] Verbridge, S.S., Craighead, H.G., & Parpia, J.M. A megahertz nanomechanical resonator with room temperature quality factor over a million. *Applied Physics Letters, **92**(1), 013112 (2008).*
[59] Schmid, S., Jensen, K.D., Nielsen, K.H., & Boisen, A. Damping mechanisms in high-Q micro and nanomechanical string resonators. *Physical Review B, **84**(16), 165307 (2011).*
[60] Unterreithmeier, Q.P., Weig, E.M., & Kotthaus, J.P. Universal transduction scheme for nanomechanical systems based on dielectric forces. *Nature, **458**(7241), 1001 (2009).*
[61] Kermany, A.R., et al. Microresonators with Q-factors over a million from highly stressed epitaxial silicon carbide on silicon. *Applied Physics Letters, **104**(8), 081901 (2014).*